

The symmetry problem of the *Fermi* and eROSITA bubbles: A proof-of-concept study

Po-Hsun Tseng^{1*}  H.-Y. Karen Yang^{2,3,4†}  Hsi-Yu Schive^{1,5,6,4‡}  Chun-Yen Chen⁷ Tzihong Chiueh^{1,5,6§} 

¹*Institute of Astrophysics, National Taiwan University, Taipei 10617, Taiwan*

²*Institute of Astronomy, National Tsing Hua University, Hsinchu 30013, Taiwan*

³*Center for Informatics and Computation in Astronomy, National Tsing Hua University, Hsinchu 30013, Taiwan*

⁴*Physics Division, National Center for Theoretical Sciences, Taipei 10617, Taiwan*

⁵*Department of Physics, National Taiwan University, Taipei 10617, Taiwan*

⁶*Center for Theoretical Physics, National Taiwan University, Taipei 10617, Taiwan*

⁷*Institute of physics, National Taiwan University, Taipei 10617, Taiwan*

13 March 2022

ABSTRACT

The *Fermi* Gamma-Ray Space Telescope reveals two large bubbles in the Galaxy, which extend nearly symmetrically $\sim 50^\circ$ on either side of the Galactic center (GC). The recent discovery of giant eROSITA bubbles also shows a symmetrically enhanced X-ray emission from the shells around the eROSITA bubbles. To this end, previous simulation-based works based on active galactic nucleus (AGN) jets model assumed that the jets are vertical to the Galactic disk; however, there is a lack of preferred orientation of jets with respect to the Galactic disk. Using three-dimensional (3D) special relativistic hydrodynamic (SRHD) simulations that include cosmic rays (CRs) and thermal gas, we show that a thin interstellar medium (ISM) disk is a substantial component for the symmetric *Fermi* and eROSITA bubbles (collectively, Galactic bubbles). We also produce simulated gamma-ray and microwave spectra from the inverse Compton (IC) scattering and synchrotron, and compare them with the observed counterparts in order to verify an oblique AGN jets model. We find that (1) The simulated Galactic bubbles are nearly symmetric about the GC albeit the bipolar jets are at an angle 45° with respect to the rotation axis of the Galactic plane (disc normal hereafter). (2) The edge of the eROSITA bubbles is a forward shock, originally driven by oblique bipolar jets emanating from the GC 12.39 million years ago, and significantly stretched by the stratified atmosphere afterwards. (3) Followed by the forward shock is a hot (~ 2 keV), turbulent, and pressure-balanced plasma, which we interpret as the *Fermi* bubbles. Inside the simulated *Fermi* bubbles, there are two additional innermost bubbles we have not detected yet. The innermost bubbles are essentially a reverse shock permanently associated with the disk. (4) According to the microwave and leptonic gamma-ray spectra, the best-fitting CRe power-law index is found to be 2.4. The broad agreement between the simulations and observations, either from the point of view of their morphology or multiwavelength features, has thus released a caveat: the jets shall be vertical to the disc normal.

Key words: editorials, notices – miscellaneous

1 INTRODUCTION

The detection of the *Fermi* bubbles (Su and Finkbeiner 2012; Ackermann et al. 2014; Narayanan and Slatyer 2017), two large bubbles symmetrically extending about 50 degrees above and below the Galactic plane, is one of the great discoveries made with *Fermi* Large Area Telescope (Atwood et al. 2009).

The gamma-ray emission of the *Fermi* bubbles is observed

in the energy range of 1–100 GeV and has an almost spatially uniform hard spectrum, sharp edges and an approximately flat brightness distribution.

Over the course of a decade, the first all-sky X-ray survey with high-spatial resolution (Predehl et al. 2021) from eROSITA (Predehl et al. 2020) also reveals a giant hourglass-shaped structure (eROSITA bubbles hereafter) at the GC, extending about twice as large as the *Fermi* bubbles. The large-scale X-ray structure shows that the intrinsic size of the bubbles is 14 kpc across (Predehl et al. 2021), and displays morphological symmetry about the Galactic plane as the *Fermi* bubbles.

Their symmetry about the GC suggests that they originate

* zengbs@gmail.com

† hyang@phys.ntnu.edu.tw

‡ hyschive@phys.ntnu.edu.tw

§ chiuehth@phys.ntnu.edu.tw

from powerful energy injections from the GC, possibly related to nuclear star formation (Crocker and Aharonian 2011; Carretti et al. 2013) or past AGN activity (Guo and Mathews 2012; Yang and Ruszkowski 2017).

Early attempts (Sarkar et al. 2015; Yang and Ruszkowski 2017; Zhang and Guo 2020) to model the symmetric Galactic bubbles assumed that the jets are vertical to the Galactic plane. However, observation (Gallimore et al. 2006) has proposed that there is a lack of preferred orientation of jets with respect to the disc normal. In contrast, a number of galaxies in which the jets are oblique to the disc normal (e.g. NGC 3079, Cecil et al. 2001; NGC 1052, Dopita et al. 2015), including galaxies in which the jets lie in the plane of the disc (e.g. IC 5063, Morganti et al. 2015).

To this end, this work introduces a dense, thin disc of ISM around a jet source to deflects and decelerates the oblique jets, in an attempt to resolve the symmetry problem of the Galactic bubbles.

The main purpose of this study is to use 3D special relativistic hydrodynamics simulations involving CR jet injections from the central SMBH in the Galaxy to investigate whether the *oblique* jet scenario is able to produce the *symmetric* Galactic bubbles that are consistent with the observed features, including the shape, the surface brightness, and the spectra of *Fermi* bubbles (Ackermann et al. 2014) and of microwave haze (Dobler and Finkbeiner 2008; Ade et al. 2013).

This paper is organized as follows. In Section 2, we describe the numerical techniques and initial conditions employed. In Section 3, we first present characteristics of our simulated Galactic bubbles, and then discuss how the disk affects the formation of the bubbles. We directly compare the morphology and profile of simulated eROSITA bubbles with observed X-ray map in Section 3.2, and also present the simulated and observed multiwavelength spectra of the *Fermi* bubbles in Section 3.3. Finally, the summary and implications of our findings are given in Section 4.

2 METHODOLOGY

We used the GPU-accelerated special relativistic hydrodynamics AMR code (GAMER-SR) developed at the National Taiwan University (Schive et al. 2010, 2018; Tseng et al. 2021) to carry out the simulations of the Galactic bubbles by CR and relativistic fluid injections from the GC.

As stressed by Yang et al. (2012), CR diffusion has an insignificant effect on the overall morphology of the *Fermi* bubbles, but only sharpens the edges of the simulated bubbles by the interplay between magnetic fields and anisotropic CR diffusion with suppressed perpendicular diffusion across the bubble surface.

Moreover, the magnetic fields within the *Fermi* bubbles should be weak due to adiabatic expansion, and thus the fields has a little effect on the overall dynamics.

For these two reasons, we have ignored the CR diffusion and the magnetic field throughout the simulation. Also, we do not simulate the spectral evolution of the CR and assume the pressure ratio of CR to gas is much less than 1 so that the contribution of CR pressure gradient to the momentum of the gas can be ignored. (we will see that the pressure ratio is around 0.1–0.2 throughout the bubbles formation) Over and above, we neglect the cooling and heating processes of CRs,

such as energy losses due to synchrotron and inverse Compton emission, and CR reacceleration in shocks/turbulences.

In this approach, we treat CRs as a single species without distinction between electrons and protons, and directly evolve the CR energy density e_{cr} as a function of \mathbf{r} and t . The CRs are advected with the thermal gas, and in return the velocities of gas can react to the gradients of the CR pressure via the source term containing spatial divergence of fluid velocities.

Since the relativistic fluid ejected by the jet source is quickly stalled off and slowed down by the dense ISM in a short time, and the relativistic fluid accounts for a little minority of total mass inside the simulation box, we still use the Newtonian gravity to attack this problem.

The governing equations solving the special relativistic ideal fluid including CR advection, and dynamical coupling between the thermal gas and CRs without CR diffusion can be written a succinct form as

$$\partial_t D + \partial_j (D U^j / \gamma) = 0, \quad (1a)$$

$$\partial_t M^i + \partial_j (M^i U^j / \gamma + p_{\text{total}} \delta^{ij}) = -\rho \partial_i \Phi, \quad (1b)$$

$$\partial_t \tilde{E} + \partial_j \left[(\tilde{E} + p_{\text{gas}}) U^j / \gamma \right] = 0, \quad (1c)$$

$$\partial_t (\gamma e_{\text{cr}}) + \partial_j (\gamma e_{\text{cr}} U^j) = -p_{\text{cr}} \partial_j U^j, \quad (1d)$$

where the five conserved quantities of gas D , M^i , and \tilde{E} are the mass density, the momentum densities, and the reduced energy density, respectively. The reduced energy density is defined by subtracting the rest mass energy density of gas from the total energy density of gas. γ and U^j are the temporal and spatial component of four-velocity of gas. ρ is the gas density in the local rest frame defined by D/γ . p_{gas} is the gas pressure. p_{cr} and e_{cr} are the CR pressure and CR energy density measured in the local rest frame. p_{total} is the sum of p_{gas} and p_{cr} . Note that we simply replace p_{total} by p_{gas} in this paper as we have assumed $p_{\text{cr}} \ll p_{\text{gas}}$. Φ is a gravitational potential. c is the speed of light, and δ^{ij} is the Kronecker delta notation. Throughout this paper, Latin indices run from 1 to 3, except when stated otherwise.

The set of Equation (1) is closed by using the Taub-Mathews equation of state (Taub 1948; Mathews 1971) that approximates the exact EoS (Synge 1957) for ultra-relativistically hot gases coexisting with non-relativistically cold gases.

GAMER-SR adopts a new algorithm (Tseng et al. 2021) to convert between primitive (ρ , U^j , p) and conserved variables (D , M^j , \tilde{E}), significantly reducing numerical error caused by catastrophic cancellations that commonly occur within the regions with high Mach number flows. e.g., jet-ISM interaction zones.

GAMER-SR also adaptively and locally reduce the min-mod coefficient (Tseng et al. 2021) within the failed patch group rarely occurring in the SRHD solver, new patches allocations, and ghost-zone interpolations. In this manner, we provide an elegant approach to avoid the use of pressure/density floor, being unnatural but widely used in almost publicly available codes.

2.1 The Galactic and Disk Models

As a proof-of-concept study, we approximate conventionally axisymmetric stellar potential of Milky Way by a plane-parallel potential that is symmetric about the mid-plane, or the Galactic plane, $z = 0$ in a simulation box size of $14 \times 14 \times 28$ kpc, slightly larger than the size of eROISTA bubbles.

The plane-parallel potential is fixed throughout our simulations and given by

$$\Phi_{\text{total}}(z) = \Phi_{\text{bulge}}(z) + \Phi_{\text{halo}}(z), \quad (2)$$

where

$$\Phi_{\text{bulge}}(z) = 2\sigma_{\text{bulge}}^2 \ln \cosh \left(z \sqrt{\frac{2\pi G \rho_{\text{bulge}}^{\text{peak}}}{\sigma_{\text{bulge}}^2}} \right) \quad (3)$$

is the potential of an isothermal slab mainly contributed by stars around the Galactic bulge, and $\Phi_{\text{halo}}(z) = v_{\text{halo}}^2 \ln(z^2 + d_{\text{h}}^2)$ is a plane-parallel dark logarithmic halo potential.

With the help of the isothermal and hydrostatic equilibrium conditions, and assuming the interfaces between the isothermal disc and atmosphere are in thermal pressure equilibrium, we can write the steady-state gaseous density distribution, confined in the total potential, of the disc and Galactic atmosphere as

$$\rho_{\text{isoDisk}}(z) = \rho_{\text{isoDisk}}^{\text{peak}} \exp \left[-\frac{\Phi_{\text{total}}(z)}{k_B T_{\text{isoDisk}}/m_p} \right], \quad \text{if } |z| < z_0, \quad (4a)$$

$$\rho_{\text{atmp}}(z) = \rho_{\text{atmp}}^{\text{peak}} \exp \left[-\frac{\Phi_{\text{total}}(z)}{k_B T_{\text{atmp}}/m_p} \right], \quad \text{otherwise,} \quad (4b)$$

where m_p is the proton mass, T_{isoDisk} and T_{atmp} is the temperature of the isothermal disc and atmosphere, $\rho_{\text{isoDisk}}^{\text{peak}}$ and $\rho_{\text{atmp}}^{\text{peak}}$ is the peak mass density of the disc and atmosphere on the mid-plane $z = 0$.

We tabulate parameters in the first four categories of Table 1, except for $\rho_{\text{atmp}}^{\text{peak}}$ that can be derived from the other known parameters and thermal pressure equilibrium condition on the interfaces ($z = \pm z_0$) between the disc and atmosphere.

The density profile of Equation (4) is shown in Figure 1. Beyond the core radius (~ 2 kpc) the gaseous density decreases rapidly as a power-law.

The density profile of Equation (4) is shown in Figure 1 and compared to the observed result (Miller and Bregman 2013) beyond 1 kpc.

Note that there is a difficulty in disentangling the contribution of the Local Bubble, a supernova remnant in which the Solar System is embedded (Snowden et al. 1990), and the contribution from solar wind charge-exchange processes, which produce soft X-ray emission throughout the Solar System. As a result, the density profile of the Galactic halo remains unclear (Bland-Hawthorn and Gerhard 2016).

To quantify the synchrotron radiation as a function of position, we adopt the default exponential magnetic field in GALPROP (Strong et al. 2007) that obeys the following spatial dependence:

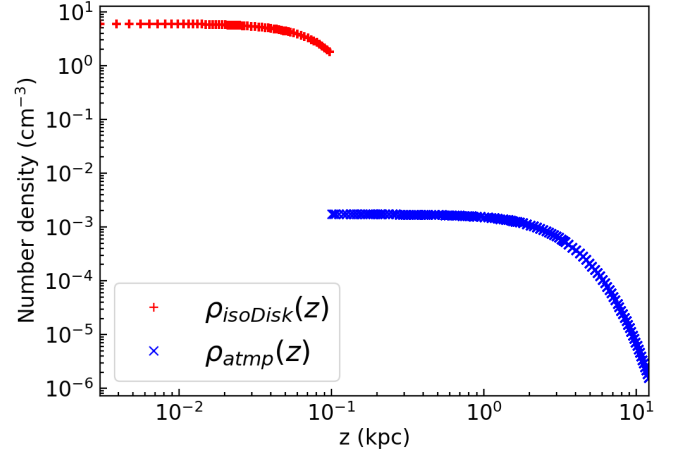


Figure 1. The density profile of the isothermal disc (red pluses) and atmosphere (blue crosses) along the positive z -axis. The density distribution is derived from hydrostatic equilibrium, the interface ($z = 0.1$) between the isothermal disc and the atmosphere is pressure balanced.

$$|\mathbf{B}(R, z)| = B_0 \exp \left[-\frac{z}{z_0} \right] \exp \left[-\frac{R}{R_0} \right], \quad (5)$$

where $R = \sqrt{x^2 + y^2}$, B_0 is the average field strength at the GC, and z_0 and R_0 are the characteristic scales in the vertical and radial directions, respectively. We adopt $z_0 = 2$ kpc and $R_0 = 10$ kpc, which are best-fitting values in the GALPROP model to reproduce the observed large-scale 408 MHz synchrotron radiation in the Galaxy. We choose $B_0 = 50$ μG based on the observed field strength at the GC (Crocker et al. 2010).

2.2 The Clumpy Multiphase Interstellar Medium

A crucial component in our work is the clumpy ISM disc initialized by the publicly available pyFC code ¹.

pyFC randomly generates dimensionless 3D scalar field $f(\mathbf{x})$ that obeys the log-normal probability distribution with mean μ and dispersion σ , and follows the power-law Kolmogorov spectrum

$$D(\mathbf{k}) = \int k^2 \hat{f}(\mathbf{k}) \hat{f}^*(\mathbf{k}) d\Omega \propto k^{-\beta}, \quad (6)$$

where $\hat{f}(\mathbf{k})$ is the Fourier transform of $f(\mathbf{x})$. The spectrum $D(\mathbf{k})$ in the Fourier space is characterized by a power-law index $\beta = 5/3$, a Nyquist limit k_{max} , and a lower cutoff wave number k_{min} . k_{max} is one-half of the spatial resolution within the disc, and k_{min} is 375.0, corresponding to the maximum size of an individual clump ~ 20 pc. Lewis and Austin (2002) and Wagner et al. (2012) have outlined a detailed procedure for constructing a clumpy scalar field, and we do not repeat here.

The density of the clumpy disc can thus be obtained by taking the scalar products of $f(\mathbf{x})$ with $\rho_{\text{isoDisk}}(z)$ over all cells within the disc, i.e., $\rho_{\text{ismDisk}}(\mathbf{x}) = f(\mathbf{x})\rho_{\text{isoDisk}}(z)$. Also, the thermal pressure equilibrium within the clumpy

¹ <https://pypi.python.org/pypi/pyFC>

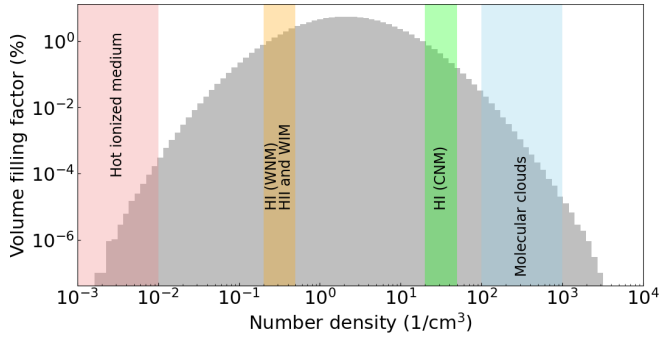


Figure 2. The volume filling factor as a function of initial number density within the disc without jet source. The vertical bands from left to right depict the allowable number densities (Ferrière 2001) for hot ionized, warm neutral (WNM), warm ionized (WIM), cold neutral mediums (CNM), and molecular clouds.

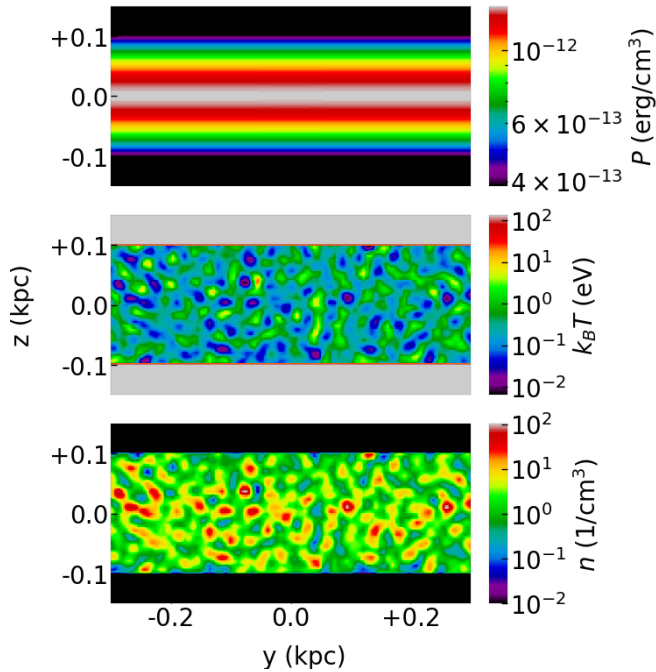


Figure 3. Close-up view of the initial pressure (top), temperature (middle), and number density (bottom) slices in the y-z plane through the center of the disc.

disc implies that the temperature of the disc is $T_{\text{ismDisk}}(\mathbf{x}) = T_{\text{isoDisk}}(z)\rho_{\text{isoDisk}}(z)/\rho_{\text{ismDisk}}(\mathbf{x})$.

The last category in Table 1 summarize the parameters of the clumpy disc and their references.

On the basis of this setup, we cover the AMR base level with $16 \times 16 \times 32$ root cells, refined progressively on the mid-plane $z = 0$ based on the gradient of mass density. We also restrict the refinement level at 7 within the disc so that a molecular cloud can be adequately resolved by approximately 30 cells along their diameter, 20 pc.

In this way, we plot the volume filling factor as a function of initial number density within the disc without the jet source in Figure 2, and show a close-up view of the pressure, temperature, and number density slices in the y-z plane through the center of the disc in Figure 3.

2.3 Oblique jets injection

We simulate the jet with an inclination angle 45° with respect to the Galactic plane in order to release the caveat that the jet direction must be perpendicular to the Galactic plane, and in particular to investigate how the dense disc affect the bubbles formation.

A few additional quantities are used to characterize the jets: the density contrast between the thermal gas contained in the jet source and the atmosphere gas, $\rho_{\text{jet}}/\rho_{\text{amb}} = 10^{-3}$, the temperature contrast, $T_{\text{jet}}/T_{\text{amb}} = 2 \times 10^4$, the pressure ratio of CR to gas is 0.18, and the flow 4-velocity inside the jet source $\beta\gamma = 0.6$ along the symmetric axis of cylinder. The jet power is thus 3.2×10^{42} erg/s, resulting in the Eddington ratio 0.008.

Note that as we inject the jets at the center of the clumpy disc, we define the atmosphere gas density by the peak density of the isothermal disc on the mid-plane $z = 0$ (i.e. $\rho_{\text{isoDisk}}^{\text{peak}}$), as opposed to the *clumpy* density around the jet source, to avoid ambiguous definition.

The bipolar jets are constantly ejected from a cylindrical source at the beginning of simulation ($t = 0$) and suddenly quenched at $t = 1.2$ Myr before fully breaking out the disc. Without quenching, the Galactic bubbles at the present time will be asymmetric about the Galactic plane. The jet duration allows the total ejected energy to be 1.2×10^{56} erg between 8×10^{55} erg and 1.3×10^{56} erg, estimated by Predehl et al. (2020).

The diameter and height of cylindrical source are 4 pc, leading to the source volume ($\sim 50 \text{ pc}^3$) is much smaller than that of an individual clump by a factor of about 83. By intentionally reducing the volume ratio of the jet source to an individual clump, we can mitigate the effect of the randomness of the clumps on the bubbles. Moreover, we resolve the jet source with the highest refinement level 11, bringing the finest spatial resolution up to 0.4 pc.

3 RESULTS

3.1 Morphology and properties of Galactic bubbles

Figure 1 shows the slices of pressure (top), temperature (middle), number density (bottom) at the end of simulation $t = 12.39$ Myr. The slices pass through the bipolar jet source injecting along $z = -y$ direction.

The fiducial run (Section 3.1) with the initial condition specified in Section 2 shows that the edge of the outermost bubbles is indeed a forward shock, expanding 12.5 kpc above and below the Galactic plane, with a semiminor axis about 6.8 kpc on the plane. We note that the overall extent of the outermost bubbles is comparable to the two spherical objects of a radius 6-7 kpc proposed by Predehl et al. (2020) for modeling the eROSITA bubbles based on X-ray emissions.

The temperature profile (left middle panel in Figure 1) along the positive z-axis in Figure 1 indicates that the smooth region (purple band in Figure 1) emitting X-ray is around 0.3-0.5 keV, similar to that observed by Miller and Bregman (2016) and Kataoka et al. (2018).

Followed by the forward shock is a turbulent and hot plasma in pressure balance with the external medium. As shown in the temperature or density slices of the fiducial run, the full extent of the turbulent plasma is 9 kpc, fairly close

[t]

Table 1. Parameters of the disc, atmosphere, and gravitational potential in the simulations.

Parameter	Description	Value	Reference
Static stellar potential			
σ_{bulge}	Velocity dispersion of bulge	100 km.s ⁻¹	(Valenti et al. 2018)
$\rho_{\text{bulge}}^{\text{peak}}$	Peak average density of bulge	4×10^{-24} g.cm ⁻³	N/A
Static dark halo potential			
v_{halo}	Characteristic velocity	131.5 km.s ⁻¹	(Johnston et al. 1995)
d_{h}	Core radius	12 kpc	"
Atmosphere			
T_{atmp}	Temperature of atmosphere	10 ⁶ K	(Tepper-García et al. 2015)
Isothermal disc			
z_0	Scale height of disc	100 pc	(Ferrière 2001)
T_{isoDisk}	Temperature of disc	10 ³ K	"
$\rho_{\text{isoDisk}}^{\text{peak}}$	Peak mass density of disc	10^{-23} g.cm ⁻³	"
Clumpy disc			
$\dagger k_{\text{min}}$	Cutoff wave number	375.0	(Ferrière 2001)
μ	Mean of scalar field	1.0	N/A
$\ddagger \sigma$	Dispersion of scalar field	5.0	(Federrath et al. 2010)
β	Power law index	-5/3	N/A

$\dagger k_{\text{min}} = 375.0$ leads to the size of an individual molecular cloud ~ 100 pc.

\ddagger In numerical simulations of turbulence, Federrath et al. (2010) find $\sigma \sim 3.6$ and 35 for solenoidal (divergence-free) and compressive (curl-free) driving force, respectively, so that our adopted value of 5 is closer to their solenoidal result.

to that of the observed *Fermi* bubbles (Su et al. 2010). Also, the temperature of the plasma is as high as 2 keV, comparable to few keV inside the *Fermi* bubbles by observing X-ray absorption lines through the hot gaseous halo along many different sight lines in the sky (Miller and Bregman 2013). The general agreement of extent and temperature suggests that the *Fermi* bubbles is essentially a turbulence rather than a smooth shock (Zhang and Guo 2020).

The most interesting finding is that there are innermost bubbles (dashed box in the top panel of Section 3.1) extending out from the GC on either side of the thin disk. The innermost bubbles are cold (1-10 eV), dense (10^{-4} – 10^{-2} cm⁻³), and underpressured with respect to the turbulent plasma.

Moreover, the close-up view (right column in ??) of profiles and slices (Figure 5) demonstrates that the pressure rises dramatically outward across the edge of the innermost bubbles, indicating that the innermost bubbles are an expanding reverse shock. The high density upstream of the reverse shock requires an even higher density downstream. Continuing outward, the higher density must match with low density further downstream; thus there exists a dense shell.

The turbulent plasma is therefore bracketed between the downstream of reverse shock and of the outermost forward shock, thus heating the turbulent plasma up considerably.

We stressed that either the outermost, turbulent plasma, or innermost bubbles are symmetric about the Galactic plane despite the jet is tilted to the disk normal at an angle 45°.

?? shows the slices of various gas properties at $t = 12.39$ Myr, including pressure (top), temperature (middle), density (bottom) with the same jet source as the fiducial run but in different Galactic environments.

We compare the clumpy disk (Section 3.1) with the smooth disc (Section 3.1), specified by the initial density profile shown in Figure 1, in a stratified atmosphere. The results

show that the initial density distribution of the dense disc has an insignificant effect on the overall dynamics of bubbles. However, the outermost bubbles arising from the smooth disc in an uniform atmosphere (Section 3.1) is spherical-shape, suggesting the stratification facilitates the outermost bubbles elongation significantly. Also, Section 3.1 reveal that the development of the innermost bubbles is always associated with the disc, without the disc, the outermost bubbles and the turbulent plasma will be oblique, indicating the dense disc is crucial for the symmetry of the Galactic bubbles and for the innermost bubbles formation.

3.2 X-ray

The X-ray emissivity is computed for each computational volume cell using the MEKAL model (Mewe et al. 1985; Kaastra and Mewe 1993; Liedahl et al. 1995) implemented in the utility XSPEC (Arnaud 1996), assuming solar metallicity. The X-ray intensity map are then generated by projecting the emissivities along lines of sight pointing away from the solar position at $(R_{\odot}, 0, 0) = (8, 0, 0)$ kpc with angular resolutions of 0.5 degrees, where R_{\odot} is the Sun-GC distance.

We point out that the projections throughout this paper is ‘perspective’, which has the effect of making distant object appear smaller than the same object in the near distance, in order to facilitate a reliable interpretation of simulated all-sky map, and also that the observed X-ray emission is contributed by all the gas in the Milky Way halo, which likely extends to a radius of ~ 250 kpc (Blitz and Robishaw 2000; Grcevich and Putman 2009), much bigger than our simulation box.

We first compute the X-ray emissivity from the simulated gas within a radius of 25 kpc away from the GC. Then, beyond 25 kpc the gas is assumed to be isothermal with $T = 10^6$

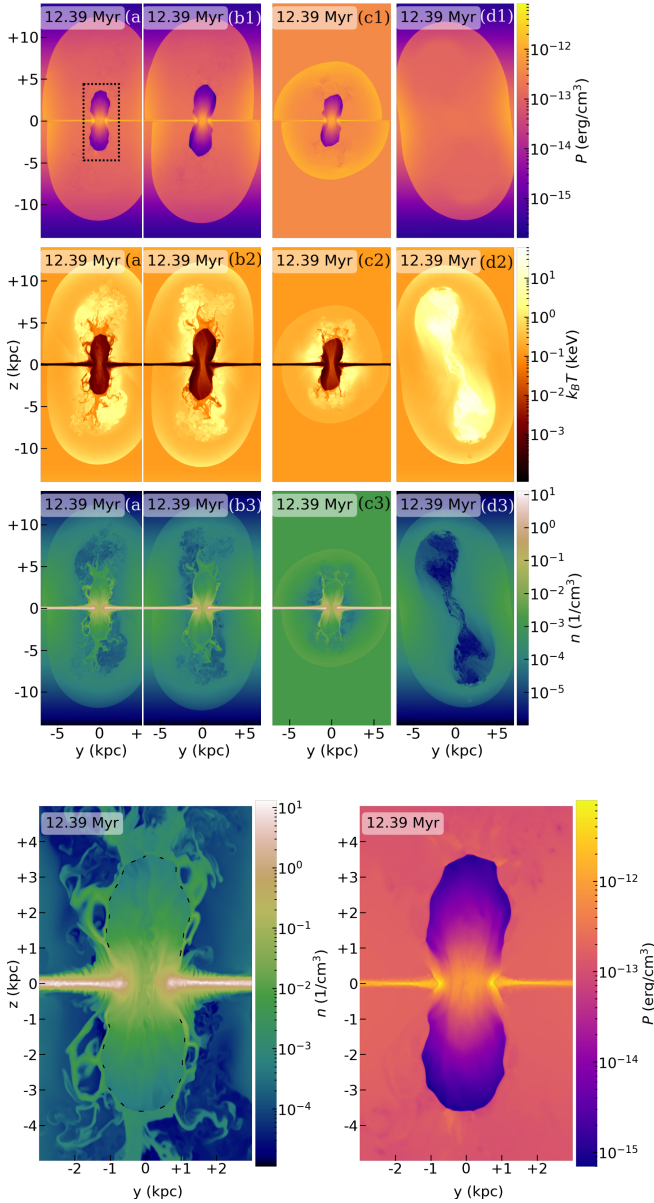


Figure 5. Zoom-in images of the density (left) and pressure (right) slices of the innermost bubbles. The high density upstream of the reverse shock requires an even higher density downstream. Continuing outward, the higher density must match with low density further downstream; thus there exists a dense shell (the turbulent region outside the black dashed line on density slice).

K and follows out to a radius of 250 kpc the observed density profile of (Tepper-García et al. 2015).

?? shows the comparison between simulated (top) and observed (bottom) all-sky map in the range 0.6–1.0 keV at 12.39 Myr and the present time, respectively. In the simulated map, the red arrow at the center of map represents the direction of the bipolar jet, constantly ejecting at an angle of 45° to the disc normal between 0–1.2 Myr.

?? displays the simulated count rate profiles (red) in the same energy band as ?? cut at various galactic latitudes (as labelled), compared with the observation (black). ?? is quite revealing in several ways.

First, we observe that The simulated eROSITA bubbles

are not as limb-brightened as the observation. A possibility to enhance the X-ray emission is to include shock-accelerated CRs near the shock, in which CRs could increase the compressibility of the fluid, resulting in the enhanced thermal Bremsstrahlung emissivity that is proportional to density squared. The broad agreement between simulated and observed X-ray maps hints that the full vertical extent of the eROSITA bubbles can be properly formed by an oblique jet within a thin disk of dense ISM.

Second, as shown in ??, the half-width of the outermost bubbles is around 7 kpc, corresponding to an half angular width $\sin^{-1}(7 \text{ kpc}/R_\odot) \sim 122^\circ$, which is as wide as the eROSITA bubbles in the simulated X-ray map (top panel in ??). We therefore suggest that the eROSITA bubble shells are a signature of compressed forward shocks that have been driven into the northern and the southern Galactic halo, as previously proposed by Predehl et al. (2020).

Third, the innermost bubbles shown in ??, even though with high column density, are invisible in the simulated X-ray map as the temperature of the innermost bubbles is around 1–10 eV (see the temperature profile in ??). Consequently, the X-ray emission within the innermost bubbles is severely suppressed by the cutoff $\exp[-h\nu/k_B T]$ in the thermal Bremsstrahlung emissivity. This is the reason why the innermost bubbles are unseen in the X-ray observation.

3.3 Gamma-ray and microwave spectra: constraint on the CRe spectral index

In this section, we give the constraint on the CRe spectral index by comparing the simulated gamma-ray and microwave spectra with the observed spectra of the Fermi bubbles (Ackermann et al. 2014) and the microwave haze (Dobler and Finkbeiner 2008), respectively.

The simulated gamma-ray and microwave spectra is based on the IC scattering and synchrotron, respectively, from CRe. The CRe spectrum follows a power-law distribution ranging from 0.5 MeV to 562.1 GeV.

The IC emissivity of the upscattered photons at the energy ϵ_1 is computed for each computational cell in our simulations using the Klein-Nishina IC cross-section (Jones 1968; Blumenthal and Gould 1970) to handle the scattering between ultra-relativistic CRe and photons in the ISRF:

$$\frac{dE}{dt d\epsilon_1 dV} = \frac{3}{4} \sigma_T c \mathbb{C} \epsilon_1 \int_{\epsilon_{\min}}^{\epsilon_{\max}} \frac{n(\epsilon)}{\epsilon} d\epsilon \int_{\gamma_{\min}(\epsilon)}^{\gamma_{\max}} \gamma^{-(p+2)} f(q, \Gamma) d\gamma, \quad (7a)$$

$$f(q, \Gamma) =$$

$$2q \ln q + (1 + 2q)(1 - q) + 0.5(1 - q) \frac{(\Gamma q)^2}{1 + \Gamma q}, \quad (7b)$$

$$q = \frac{\epsilon_1 / \gamma m_e c^2}{\Gamma (1 - \epsilon_1 / \gamma m_e c^2)}, \quad (7c)$$

$$\Gamma = \frac{4\epsilon\gamma}{m_e c^2}, \quad (7d)$$

$$\gamma_{\min}(\epsilon) = 0.5 \left(\frac{\epsilon_1}{m_e c^2} + \sqrt{\left(\frac{\epsilon_1}{m_e c^2} \right)^2 + \frac{\epsilon_1}{\epsilon}} \right), \quad (7e)$$

where σ_T is the Thomson cross section, c speed of light, m_e electron mass, $n(\epsilon)$ the energy distribution of the photon number density in ISRF given by Porter et al. (2017), γ the Lorentz factor of CRe, \mathbb{C} and p are the normalization constant and spectral index of CRe power-law spectrum. $\gamma_{\min}(\epsilon)$ is the minimum Lorentz factor of CRe that allows incident photons to scatter from energy ϵ to ϵ_1 . γ_{\max} is the maximum CRe Lorentz factor in the spectrum.

We perform the double integration in Equation (7) on each cell over the range of CRe Lorentz factor, and the range of incident photon energy between $\epsilon_{\min} = 1.13 \times 10^{-4}$ eV (cosmic microwave background) and $\epsilon_{\max} = 13.59$ eV (optical starlight) to obtain the simulated IC emissivities.

The synchrotron emissivity with an isotropic electron pitch angle distribution is given by Blumenthal and Gould (1970):

$$\frac{dE}{dt d\nu dV} = \frac{4\pi \mathbb{C} e^3 B^{0.5(p+1)}}{m_e c^2} \left(\frac{3e}{4\pi m_e c} \right)^{0.5(p-1)} a(p) \nu^{-0.5(p-1)}, \quad (8a)$$

$$a(p) = \frac{2^{0.5(p-1)} \sqrt{3} \Gamma[(3p-1)/12] \Gamma[(3p+9)/12] \Gamma[(p+5)/4]}{8\sqrt{\pi}(p+1) \Gamma[(p+7)/4]}, \quad (8b)$$

where Γ is the gamma function, B is the magnetic field strength defined in Equation (5).

For a given longitude and latitude range, the simulated spectra are computed by projecting emissivities as we project X-ray emissivities in Section 3.2, and then we average the spectra over all the sight lines within the region on sky.

Figure 6 shows the simulated microwave (left) and gamma-ray (right) spectra averaged over the different patches (shown in the legends) of the sky. The row from top to bottom shows the spectra with different CRe spectral index 2.2, 2.4 and 2.6. Several points are worth specific comment.

First, we find that the simulated gamma-ray spectra are well fitted by the CRe spectral index 2.4 (the middle row), despite the simulated microwave spectra are marginally consistent with the observed.

Second, the simulated and observed gamma-ray spectra is nearly latitude independent, and characterized by a broad bump that roughly peaks around ~ 10 GeV. However, the high-latitude spectrum tends to be slightly dimmer than low-latitude probably because the optical intensity in ISRF decays with increasing latitude.

Third, the gamma-ray spectra for all latitudes indicate a spectral cutoff around energies 400–500 GeV, remarkably consistent with the observed cutoff energy. This is expected since the upscattered high-energy photons ($\epsilon_1 \sim 450$ GeV) mainly arise from the scatterings between the relativistic CRe ($\gtrsim 408$ GeV) and optical starlight ($\epsilon \sim 10$ eV). Thus, Equation (7e) can be reduced to $\epsilon_1 \sim \gamma m_e c^2$ in the Klein–Nishina limit (i.e. $\epsilon_1 \epsilon \gg (m_e c^2)^2$), implying most of the CRe energy is carried away by the upscattered photons.

Fourth, the good agreement between the simulated and observed gamma-ray/microwave spectra implies that, in the presence of ISRF and magnetic fields, the emission of the Fermi bubbles and the microwave haze can be produced by the same high-energy electrons via inverse Compton scatter-

ings and synchrotron radiations, respectively, as previously suggested (Su et al. 2010; Dobler 2012).

Figure 7 shows the simulated gamma-ray photon flux with a CRe power-law index 2.4 compared with the observed one in the energy bin 76.8–153.6 GeV. As the eROSITA bubbles, one can see that the symmetric *Fermi* bubbles can also be realized by oblique jets.

Finally, the comparison between ?? and Figure 8 shows that the CR pressure is around $5 \times 10^{-15} - 8 \times 10^{-15}$ erg/cm³, bringing the pressure ratio of CR to gas is 0.1–0.2, similar to 0.18 at the beginning of the simulation. We therefore stress that ignoring the contribution of CR pressure gradient to the momentum of the gas in Equation (1) is reasonable.

4 CONCLUSIONS

In this work, we introduce a thin, dense disk composed of clumpy ISM to divert the oblique jets at an angle 45° to the disk normal in the past energetic event of the central SMBH. We investigate the properties of the Galactic bubbles and the microwave haze using 3D special relativistic hydrodynamic simulations of CR injection from the SMBH assuming the leptonic model.

Our findings are as follows.

- The Galactic bubbles are nearly symmetric about the Galactic plane albeit the bipolar jets are at an angle 45° with respect to the disc normal. The broad agreement between simulated and observed multiwavelength features provides supporting evidence for the oblique jet scenario, and also releases the caveat given by earlier simulation-based studies: the jets shall be vertical to the disc normal.
- The randomness of clumpy disk has a insignificant impact on the overall dynamic of the Galactic bubbles. The development of the reverse shocks (the innermost bubbles) is always associated with the dense disc, without the disc, the outermost bubbles and the turbulent plasma will be oblique, indicating the dense disc is crucial for the symmetry of the Galactic bubbles and for the innermost bubbles formation.
- The edge of the eROSITA bubbles is a forward shock, originally driven by oblique bipolar jets emanating from the GC 12.39 million years ago, and significantly stretched by the stratified atmosphere afterwards. The simulated eROSITA bubbles are not as limb-brightened as the observation. A possibility to enhance the X-ray emission is to include shock-accelerated CRs near the shock, in which CRs could increase the compressibility of the fluid, resulting in the enhanced thermal Bremsstrahlung emissivity that is proportional to density squared.
- Followed by the forward shock is a turbulent and hot plasma (~ 2 keV), which we interpret as the *Fermi* bubbles. The similarity of the morphology, temperature, and gamma-ray spectrum between simulated and observed *Fermi* bubbles suggests that the *Fermi* bubbles are essentially a turbulent and high temperature plasma in pressure balance with external medium. Associated with the Galactic magnetic field will lead to the stochastic acceleration of CRe, possibly in balance with the IC and synchrotron cooling. We will investigate the competition between stochastic acceleration and radiative cooling in a future work.
- According to the microwave and leptonic gamma-ray

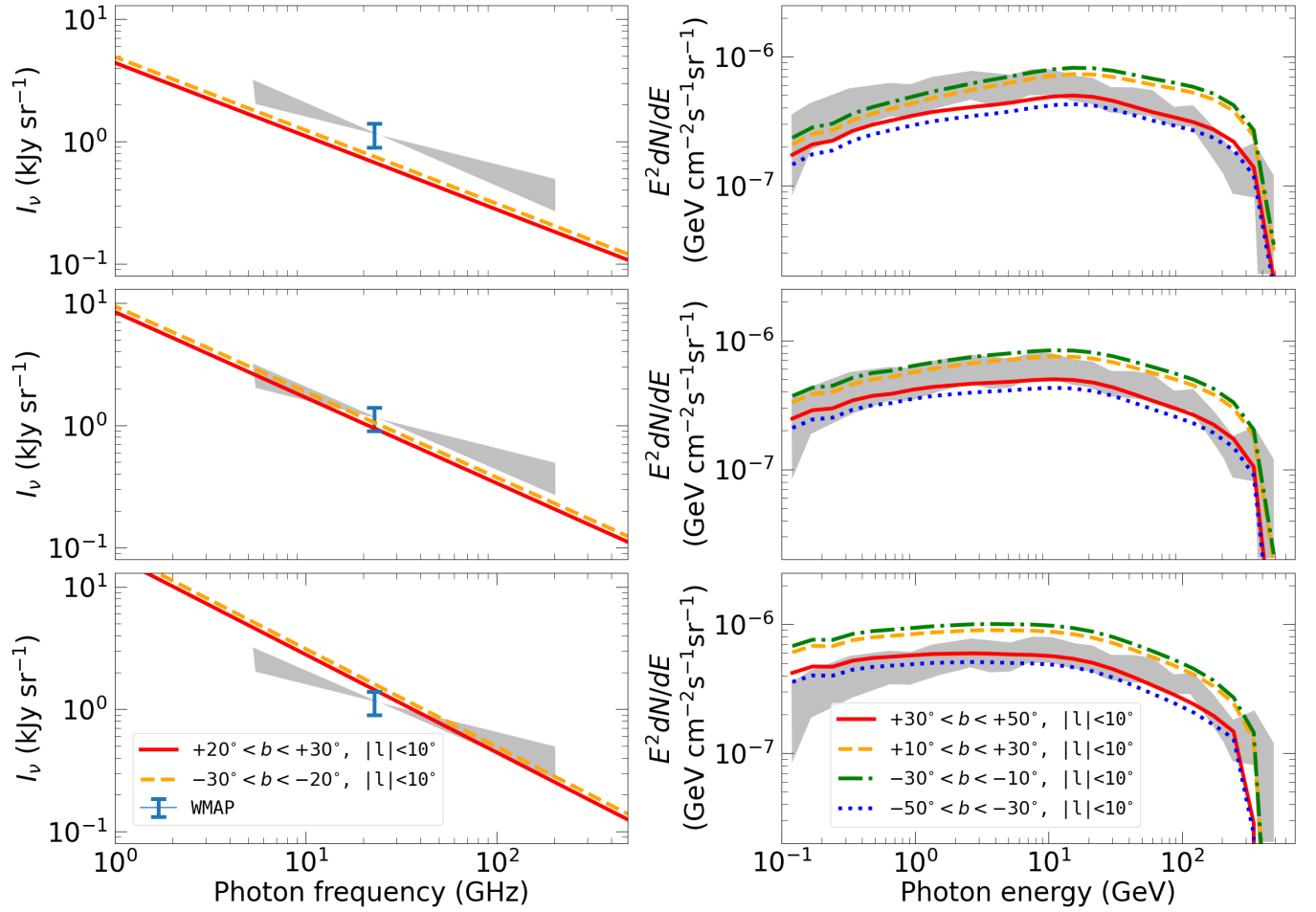


Figure 6. Simulated microwave spectra (colored lines in left) averaged over $20^\circ < |b| < 30^\circ$, $|l| < 10^\circ$. The data point represents the *WMAP* data in the 23 GHz K band and the shaded bow-tie area indicates the range of synchrotron spectral indices allowed for the *WMAP* haze (Dobler and Finkbeiner 2008). Simulated gamma-ray spectra (colored lines in right column) of the *Fermi* bubbles calculated for a longitude range of $|l| < 10^\circ$ for different latitude bins. The gray band represents the observational data of Ackermann et al. (2014). The row from top to bottom shows the microwave (left) and gamma-ray (right) spectra with CRe spectral index 2.2, 2.4 and 2.6, respectively. The CRe cutoff energy is 562.1 GeV in all cases.

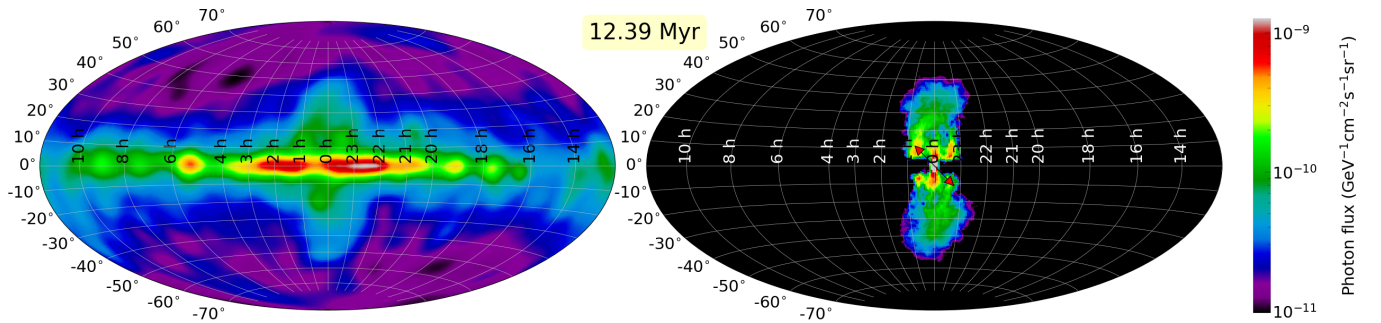


Figure 7. The observed (left; Selig et al. 2015) and simulated (right) photon flux in the energy bin 76.8 – 153.6 GeV. Note that the left panel is the photon flux of the diffuse component reconstructed by the D³PO algorithm (Selig et al. 2015) that analyzes the photon data from the *Fermi* Large Area Telescope (Atwood et al. 2009) and removes the contribution from point-like component. The red arrow at the center of the right panel depicts the direction of the bipolar jet, constantly ejecting at an angle of 45° to the disc normal in 1.2 Myr.

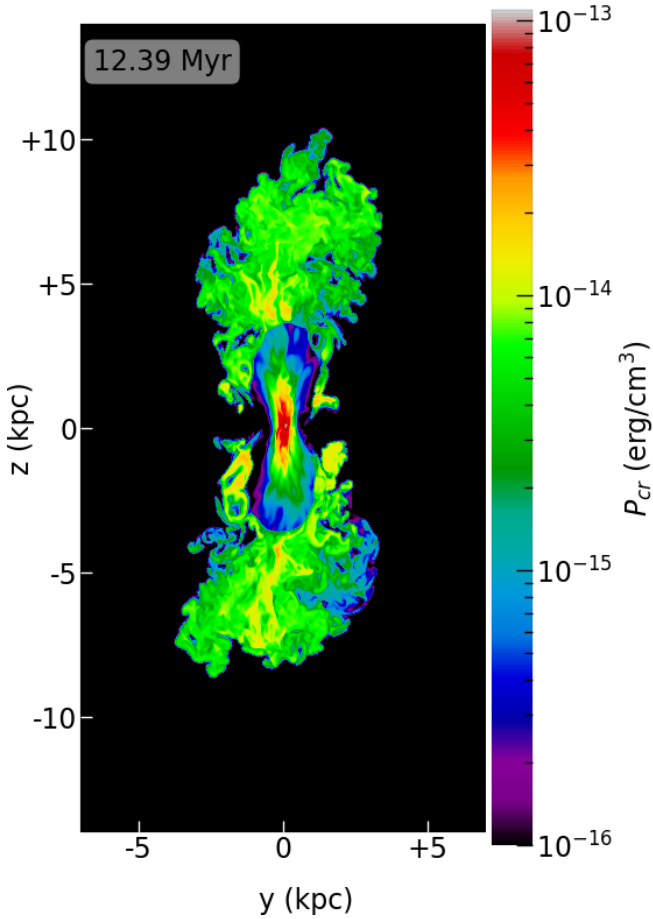


Figure 8. The CR pressure slice passing through the jet source at 12.39 Myr. Comparison between gas pressure (??) and cosmic ray pressure shows that the CR pressure is around $5 \times 10^{-15} - 8 \times 10^{-15}$ erg/cm³, bringing the pressure ratio of CR to gas is 0.1–0.2, similar to 0.18 at the beginning of the simulation. We therefore stress that ignoring the contribution of CR pressure gradient to the momentum of the gas in Equation (1) is reasonable.

spectra, the best-fitting CRe power-law index is found to be 2.4.

- The same leptotonic CRe can simultaneously account for the *Fermi* bubbles and haze emission suggested that they are physically related around the GC, and that the magnetic fields within the bubbles are close to the exponentially distributed Galactic magnetic field.

5 ACKNOWLEDGEMENTS

The authors thank Mateusz Ruszkowski and Ellen G. Zweibel for insightful comments. We thank Peter Predehl for providing the range of observed X-ray intensity in ???. A part of the simulations are performed and analyzed using computing resources operated by the National Center for High-Performance Computing (NCHC). HYKY acknowledges support from Yushan Scholar Program of the Ministry of Education of Taiwan and Ministry of Science and Technology of Taiwan (MOST 109-2112-M-007-037-MY3). HS acknowledges funding support from the Jade Mountain Young Scholar Award No. NTU-109V0201, sponsored by the Min-

istry of Education, Taiwan. This research is partially supported by the Ministry of Science and Technology of Taiwan (MOST) under grants MOST 107-2119-M-002-036-MY3 and MOST 108-2112-M-002-023-MY3, and the NTU Core Consortium project under grants NTU-CC-108L893401 and NTU-CC-108L893402.

DATA AVAILABILITY

The data underlying this article are available in the article and in its online supplementary material.

REFERENCES

- M. Ackermann, A. Albert, W. B. Atwood, L. Baldini, J. Ballet, G. Barbiellini, D. Bastieri, R. Bellazzini, E. Bissaldi, R. D. Blandford, E. D. Bloom, E. Bottacini, T. J. Brandt, J. Bregeon, P. Bruel, R. Buehler, S. Buson, G. A. Caliendo, R. A. Cameron, M. Caragiulo, P. A. Caraveo, E. Cavazzuti, C. Cecchi, E. Charles, A. Chekhtman, J. Chiang, G. Chiaro, S. Ciprini, R. Claus, J. Cohen-Tanugi, J. Conrad, S. Cutini, F. D’Ammando, A. de Angelis, F. de Palma, C. D. Dermer, S. W. Digel, L. D. Venere, E. do Couto e Silva, P. S. Drell, C. Favuzzi, E. C. Ferrara, W. B. Focke, A. Franckowiak, Y. Fukazawa, S. Funk, P. Fusco, F. Gargano, D. Gasparini, S. Germani, N. Giglietto, F. Giordano, M. Giroletti, G. Godfrey, G. A. Gomez-Vargas, I. A. Grenier, S. Guiriec, D. Hadasch, A. K. Harding, E. Hays, J. W. Hewitt, X. Hou, T. Jogler, G. Jóhannesson, A. S. Johnson, W. N. Johnson, T. Kamae, J. Kataoka, J. Knödseder, D. Kocevski, M. Kuss, S. Larsson, L. Latronico, F. Longo, F. Loparco, M. N. Lovellette, P. Lubrano, D. Malyshev, A. Manfreda, F. Massaro, M. Mayer, M. N. Mazziotta, J. E. McEnery, P. F. Michelson, W. Mitthumsiri, T. Mizuno, M. E. Monzani, A. Morselli, I. V. Moskalenko, S. Murgia, R. Nemmen, E. Nuss, T. Ohsugi, N. Omodei, M. Orienti, E. Orlando, J. F. Ormes, D. Paneque, J. H. Panetta, J. S. Perkins, M. Pesce-Rollins, V. Petrosian, F. Piron, G. Pivato, S. Rainò, R. Rando, M. Razzano, S. Razzaque, A. Reimer, O. Reimer, M. Sánchez-Conde, M. Schaal, A. Schulz, C. Sgrò, E. J. Siskind, G. Spandre, P. Spinelli, L. Stawarz, A. W. Strong, D. J. Suson, M. Tahara, H. Takahashi, J. B. Thayer, L. Tibaldo, M. Tinivella, D. F. Torres, G. Tosti, E. Troja, Y. Uchiyama, G. Vianello, M. Werner, B. L. Winer, K. S. Wood, M. Wood, and G. Zaharijas. THE SPECTRUM AND MORPHOLOGY OF THE FERMI BUBBLES. *The Astrophysical Journal*, 793(1):64, Sept. 2014. doi:10.1088/0004-637x/793/1/64. URL <https://doi.org/10.1088/0004-637x/793/1/64>.
- P. A. R. Ade, N. Aghanim, M. Arnaud, M. Ashdown, F. Atrio-Barandela, J. Aumont, C. Baccigalupi, A. Balbi, A. J. Banday, R. B. Barreiro, J. G. Bartlett, E. Battaner, K. Benabed, A. Benoît, J.-P. Bernard, M. Bersanelli, A. Bonaldi, J. R. Bond, J. Borrill, F. R. Bouchet, C. Burigana, P. Cabella, J.-F. Cardoso, A. Catalano, L. Cayón, R.-R. Chary, L.-Y. Chiang, P. R. Christensen, D. L. Clements, L. P. L. Colombo, A. Coulais, B. P. Crill, F. Cuttaia, L. Danese, O. D’Arcangelo, R. J. Davis, P. de Bernardis, G. de Gasperis, A. de Rosa, G. de Zotti, J. Delabrouille, C. Dickinson, J. M. Diego, G. Dobler, H. Dole, S. Donzelli, O. Doré, U. Dörl, M. Douspis, X. Dupac, G. Efstathiou, T. A. Enßlin, H. K. Eriksen, F. Finelli, O. Forni, M. Frailis, E. Franceschi, S. Galeotta, K. Ganga, M. Girard, G. Giardino, J. González-Nuevo, K. M. Górski, S. Gratton, A. Gregorio, A. Gruppiso, F. K. Hansen, D. Harrison, G. Helou, S. Henrot-Versillé, C. Hernández-Monteagudo, S. R. Hildebrandt, E. Hivon, M. Hobson, W. A. Holmes,

- A. Hornstrup, W. Hovest, K. M. Huppenberger, T. R. Jaffe, T. Jagemann, J. Jewell, W. C. Jones, M. Juvela, E. Keihänen, J. Knoche, L. Knox, M. Kunz, H. Kurki-Suonio, G. Lagache, A. Lähteenmäki, J.-M. Lamarre, A. Lasenby, C. R. Lawrence, S. Leach, R. Leonardi, P. B. Lilje, M. Lindén-Vørnle, M. López-Caniego, P. M. Lubin, J. F. Macías-Pérez, B. Maffei, D. Maino, N. Mandolesi, M. Maris, D. J. Marshall, P. G. Martin, E. Martínez-González, S. Masi, M. Massardi, S. Matarrese, F. Matthai, P. Mazzotta, P. R. Meinhold, A. Melchiorri, L. Mendes, A. Mennella, S. Mitra, A. Moneti, L. Montier, G. Morgante, D. Munshi, J. A. Murphy, P. Naselsky, P. Natoli, H. U. Nørgaard-Nielsen, F. Novello, D. Novikov, I. Novikov, S. Osborne, F. Pajot, R. Paladini, D. Paoletti, B. Partridge, T. J. Pearson, O. Perdereau, F. Perrotta, F. Piacentini, M. Piat, E. Pierpaoli, D. Pietrobon, S. Plaszczynski, E. Pointecouteau, G. Polenta, N. Ponthieu, L. Popa, T. Poutanen, G. W. Pratt, S. Prunet, J.-L. Puget, J. P. Rachen, R. Rebolo, M. Reinecke, C. Renault, S. Ricciardi, T. Riller, I. Ristorcelli, G. Rocha, C. Rosset, J. A. Rubiño-Martín, B. Rusholme, M. Sandri, G. Savini, B. M. Schaefer, D. Scott, G. F. Smoot, L. Spencer, F. Stivoli, R. Sudiwala, A.-S. Suur-Uski, J.-F. Sygnet, J. A. Tauber, L. Terenzi, L. Toffolatti, M. Tomasi, M. Tristram, M. Türlér, G. Umana, L. Valenziano, B. V. Tent, P. Vielva, F. Villa, N. Vittorio, L. A. Wade, B. D. Wandelt, M. White, D. Yvon, A. Zacchei, and A. Zonca. Planckintermediate results. *Astronomy & Astrophysics*, 554: A139, June 2013. doi:10.1051/0004-6361/201220271. URL <https://doi.org/10.1051/0004-6361/201220271>.
- K. A. Arnaud. XSPEC: The First Ten Years. In G. H. Jacoby and J. Barnes, editors, *Astronomical Data Analysis Software and Systems V*, volume 101 of *Astronomical Society of the Pacific Conference Series*, page 17, Jan. 1996.
- W. B. Atwood, A. A. Abdo, M. Ackermann, W. Althouse, B. Anderson, M. Axelsson, L. Baldini, J. Ballet, D. L. Band, G. Barbiellini, J. Bartelt, D. Bastieri, B. M. Baughman, K. Bechtol, D. Bédérède, F. Bellardi, R. Bellazzini, B. Berenji, G. F. Big-nami, D. Bisello, E. Bissaldi, R. D. Blandford, E. D. Bloom, J. R. Bogart, E. Bonamente, J. Bonnell, A. W. Borgland, A. Bouvier, J. Bregeon, A. Brez, M. Brigida, P. Bruel, T. H. Burnett, G. Busetto, G. A. Caliendo, R. A. Cameron, P. A. Caraveo, S. Carius, P. Carlson, J. M. Casandjian, E. Cavaz-zuti, M. Ceccanti, C. Cecchi, E. Charles, A. Chekhtman, C. C. Cheung, J. Chiang, R. Chipaux, A. N. Cillis, S. Ciprini, R. Claus, J. Cohen-Tanugi, S. Condamore, J. Conrad, R. Corbet, L. Corucci, L. Costamante, S. Cutini, D. S. Davis, D. Decotigny, M. DeKlotz, C. D. Dermer, A. de Angelis, S. W. Digel, E. do Couto e Silva, P. S. Drell, R. Dubois, D. Dumora, Y. Edmonds, D. Fabiani, C. Farnier, C. Favuzzi, D. L. Flat, P. Fleury, W. B. Focke, S. Funk, P. Fusco, F. Gargano, D. Gas-parrini, N. Gehrels, F.-X. Gentit, S. Germani, B. Giebels, N. Giglietto, P. Giommi, F. Giordano, T. Glanzman, G. Godfrey, I. A. Grenier, M.-H. Grondin, J. E. Grove, L. Guillemot, S. Guiriec, G. Haller, A. K. Harding, P. A. Hart, E. Hays, S. E. Healey, M. Hirayama, L. Hjalmarsdotter, R. Horn, R. E. Hughes, G. Jóhannesson, G. Johansson, A. S. John-son, R. P. Johnson, T. J. Johnson, W. N. Johnson, T. Kamae, H. Katagiri, J. Kataoka, A. Kavelaars, N. Kawai, H. Kelly, M. Kerr, W. Klamra, J. Knödseder, M. L. Kocian, N. Komin, F. Kuehn, M. Kuss, D. Landriu, L. Latronico, B. Lee, S.-H. Lee, M. Lemoine-Goumard, A. M. Lionetto, F. Longo, F. Loparco, B. Lott, M. N. Lovellette, P. Lubrano, G. M. Madejski, A. Makeev, B. Marangelli, M. M. Massai, M. N. Mazziotta, J. E. McEnery, N. Menon, C. Meurer, P. F. Michel-son, M. Minuti, N. Mirizzi, W. Mitthumsiri, T. Mizuno, A. A. Moiseev, C. Monte, M. E. Monzani, E. Moretti, A. Morselli, I. V. Moskalenko, S. Murgia, T. Nakamori, S. Nishino, P. L. Nolan, J. P. Norris, E. Nuss, M. Ohno, T. Ohsugi, N. Omodei, E. Orlando, J. F. Ormes, A. Paccagnella, D. Paneque, J. H. Panetta, D. Parent, M. Pearce, M. Pepe, A. Perazzo, M. Pesce-Rollins, P. Picozza, L. Pieri, M. Pinchera, F. Piron, T. A. Porter, L. Poupard, S. Rainò, R. Rando, E. Rapposelli, M. Raz-zano, A. Reimer, O. Reimer, T. Reposeur, L. C. Reyes, S. Ritz, L. S. Rochester, A. Y. Rodriguez, R. W. Romani, M. Roth, J. J. Russell, F. Ryde, S. Sabatini, H. F.-W. Sadrozinski, D. Sanchez, A. Sander, L. Sapozhnikov, P. M. S. Parkin-son, J. D. Scargle, T. L. Schalk, G. Scolieri, C. Sgrò, G. H. Share, M. Shaw, T. Shimokawabe, C. Shrader, A. Sierpowska-Bartosik, E. J. Siskind, D. A. Smith, P. D. Smith, G. Span-dre, P. Spinelli, J.-L. Starck, T. E. Stephens, M. S. Strickman, A. W. Strong, D. J. Suson, H. Tajima, H. Takahashi, T. Taka-hashii, T. Tanaka, A. Tenze, S. Tether, J. B. Thayer, J. G. Thayer, D. J. Thompson, L. Tibaldo, O. Tibolla, D. F. Tor-res, G. Tosti, A. Tramacere, M. Turri, T. L. Usher, N. Vilchez, V. Vitale, P. Wang, K. Watters, B. L. Winer, K. S. Wood, T. Ylinen, and M. Ziegler. THE LARGE AREA TELESCOPE ON THE FERMI GAMMA-RAY SPACE TELESCOPE MIS-SION. *The Astrophysical Journal*, 697(2):1071–1102, May 2009. doi:10.1088/0004-637x/697/2/1071. URL <https://doi.org/10.1088/0004-637x/697/2/1071>.
- J. Bland-Hawthorn and O. Gerhard. The galaxy in context: Structural, kinematic, and integrated properties. *Annual Re-view of Astronomy and Astrophysics*, 54(1):529–596, Sept. 2016. doi:10.1146/annurev-astro-081915-023441. URL <https://doi.org/10.1146/annurev-astro-081915-023441>.
- L. Blitz and T. Robishaw. Gas-rich dwarf spheroidals. 541(2): 675–687, Oct. 2000. doi:10.1086/309457. URL <https://doi.org/10.1086/309457>.
- G. R. Blumenthal and R. J. Gould. Bremsstrahlung, synchrotron radiation, and compton scattering of high-energy electrons traversing dilute gases. *Reviews of Modern Physics*, 42(2): 237–270, Apr. 1970. doi:10.1103/revmodphys.42.237. URL <https://doi.org/10.1103/revmodphys.42.237>.
- E. Carretti, R. M. Crocker, L. Staveley-Smith, M. Haverkorn, C. Purcell, B. M. Gaensler, G. Bernardi, M. J. Kesteven, and S. Poppi. Giant magnetized outflows from the centre of the milky way. *Nature*, 493(7430):66–69, Jan. 2013. doi:10.1038/nature11734. URL <https://doi.org/10.1038/nature11734>.
- G. Cecil, J. Bland-Hawthorn, S. Veilleux, and A. V. Filippenko. Jet- and wind-driven ionized outflows in the superbubble and star-forming disk of NGC 3079. *The Astrophysical Journal*, 555(1):338–355, July 2001. doi:10.1086/321481. URL <https://doi.org/10.1086/321481>.
- R. M. Crocker and F. Aharonian. Fermi bubbles: Gi-ant, multibillion-year-old reservoirs of galactic center cos-mic rays. *Phys. Rev. Lett.*, 106:101102, Mar 2011. doi:10.1103/PhysRevLett.106.101102. URL <https://link.aps.org/doi/10.1103/PhysRevLett.106.101102>.
- R. M. Crocker, D. I. Jones, F. Melia, J. Ott, and R. J. Protheroe. A lower limit of 50 microgauss for the magnetic field near the galactic centre. *Nature*, 463(7277):65–67, Jan 2010. ISSN 1476-4687. doi:10.1038/nature08635. URL <https://doi.org/10.1038/nature08635>.
- G. Dobler. A LAST LOOK AT THE MICROWAVE HAZE/BUBBLES WITH WMAP. *The Astrophysical Journal*, 750(1):17, Apr. 2012. doi:10.1088/0004-637x/750/1/17. URL <https://doi.org/10.1088/0004-637x/750/1/17>.
- G. Dobler and D. P. Finkbeiner. Extended anomalous foreground emission in the WMAP Three-year data. *The Astrophysical Journal*, 680(2):1222–1234, jun 2008. doi:10.1086/587862. URL <https://doi.org/10.1086/587862>.
- M. A. Dopita, P. Shastri, R. Davies, L. Kewley, E. Hampton, J. Scharwächter, R. Sutherland, P. Kharb, J. Jose, H. Bhatt, S. Ramya, C. Jin, J. Banfield, I. Zaw, S. Juneau, B. James, and S. Srivastava. PROBING THE PHYSICS OF NARROW LINE REGIONS IN ACTIVE GALAXIES. II. THE SIDING

- SPRING SOUTHERN SEYFERT SPECTROSCOPIC SNAP-SHOT SURVEY (s7). *The Astrophysical Journal Supplement Series*, 217(1):12, Mar. 2015. doi:10.1088/0067-0049/217/1/12. URL <https://doi.org/10.1088/0067-0049/217/1/12>.
- C. Federrath, J. Roman-Duval, R. S. Klessen, W. Schmidt, and M.-M. Low. Comparing the statistics of interstellar turbulence in simulations and observations. *Astronomy and Astrophysics*, 512:A81, Mar. 2010. doi:10.1051/0004-6361/200912437. URL <https://doi.org/10.1051/0004-6361/200912437>.
- K. M. Ferrière. The interstellar environment of our galaxy. *Rev. Mod. Phys.*, 73(4):1031–1066, Dec. 2001. doi:10.1103/revmodphys.73.1031. URL <https://doi.org/10.1103/revmodphys.73.1031>.
- J. F. Gallimore, D. J. Axon, C. P. O'Dea, S. A. Baum, and A. Pedlar. A survey of kiloparsec-scale radio outflows in radio-quiet active galactic nuclei. *The Astronomical Journal*, 132(2):546–569, June 2006. doi:10.1086/504593. URL <https://doi.org/10.1086/504593>.
- J. Grcevich and M. E. Putman. HI IN LOCAL GROUP DWARF GALAXIES AND STRIPPING BY THE GALACTIC HALO. 696(1):385–395, Apr. 2009. doi:10.1088/0004-637x/696/1/385. URL <https://doi.org/10.1088/0004-637x/696/1/385>.
- F. Guo and W. G. Mathews. THEFERMIBUBBLES. i. POSSIBLE EVIDENCE FOR RECENT AGN JET ACTIVITY IN THE GALAXY. *The Astrophysical Journal*, 756(2):181, Aug. 2012. doi:10.1088/0004-637x/756/2/181. URL <https://doi.org/10.1088/0004-637x/756/2/181>.
- K. V. Johnston, D. N. Spergel, and L. Hernquist. The disruption of the sagittarius dwarf galaxy. *The Astrophysical Journal*, 451: 598, Oct. 1995. doi:10.1086/176247. URL <https://doi.org/10.1086/176247>.
- F. C. Jones. Calculated spectrum of inverse-compton-scattered photons. *Physical Review*, 167(5):1159–1169, Mar. 1968. doi:10.1103/physrev.167.1159. URL <https://doi.org/10.1103/physrev.167.1159>.
- J. S. Kaastra and R. Mewe. X-ray emission from thin plasmas. I - Multiple Auger ionisation and fluorescence processes for Be to Zn. *A&AS*, 97(2):443–482, Jan. 1993.
- J. Kataoka, Y. Sofue, Y. Inoue, M. Akita, S. Nakashima, and T. Totani. X-ray and gamma-ray observations of the fermi bubbles and NPS/loop i structures. *Galaxies*, 6(1):27, Feb. 2018. doi:10.3390/galaxies6010027. URL <https://doi.org/10.3390/galaxies6010027>.
- G. M. Lewis and P. H. Austin. *1th Conference on Atmospheric Radiation*, 2002.
- D. A. Liedahl, A. L. Osterheld, and W. H. Goldstein. New Calculations of Fe L-Shell X-Ray Spectra in High-Temperature Plasmas. *ApJ*, 438:L115, Jan. 1995. doi:10.1086/187729.
- W. G. Mathews. The Hydromagnetic Free Expansion of a Relativistic Gas. *ApJ*, 165:147, Apr 1971. doi:10.1086/150883.
- R. Mewe, E. H. B. M. Gronenschild, and G. H. J. van den Oord. Calculated X-radiation from optically thin plasmas. V. *A&AS*, 62:197–254, Nov. 1985.
- M. J. Miller and J. N. Bregman. THE STRUCTURE OF THE MILKY WAY'S HOT GAS HALO. *The Astrophysical Journal*, 770(2):118, jun 2013. doi:10.1088/0004-637x/770/2/118. URL <https://doi.org/10.1088/0004-637x/770/2/118>.
- M. J. Miller and J. N. Bregman. THE INTERACTION OF THE FERMI BUBBLES WITH THE MILKY WAY'S HOT GAS HALO. *The Astrophysical Journal*, 829(1):9, Sept. 2016. doi:10.3847/0004-637x/829/1/9. URL <https://doi.org/10.3847/0004-637x/829/1/9>.
- R. Morganti, T. Oosterloo, J. B. R. Oonk, W. Frieswijk, and C. Tadhunter. The fast molecular outflow in the seyfert galaxy IC 5063 as seen by ALMA. *Astronomy & Astrophysics*, 580:A1, July 2015. doi:10.1051/0004-6361/201525860. URL <https://doi.org/10.1051/0004-6361/201525860>.
- S. A. Narayanan and T. R. Slatyer. A latitude-dependent analysis of the leptonic hypothesis for the fermi bubbles. *Monthly Notices of the Royal Astronomical Society*, 468(3):3051–3070, Mar. 2017. doi:10.1093/mnras/stx577. URL <https://doi.org/10.1093/mnras/stx577>.
- T. A. Porter, G. Jóhannesson, and I. V. Moskalenko. High-energy gamma rays from the milky way: Three-dimensional spatial models for the cosmic-ray and radiation field densities in the interstellar medium. *The Astrophysical Journal*, 846(1):67, Aug. 2017. doi:10.3847/1538-4357/aa844d. URL <https://doi.org/10.3847/1538-4357/aa844d>.
- P. Predehl, R. A. Sunyaev, W. Becker, H. Brunner, R. Burénin, A. Bykov, A. Cherepashchuk, N. Chugai, E. Churazov, V. Doroshenko, N. Eismont, M. Freyberg, M. Gilfanov, F. Haberl, I. Khabibullin, R. Krivonos, C. Maitra, P. Medvedev, A. Merloni, K. Nandra, V. Nazarov, M. Pavlinsky, G. Ponti, J. S. Sanders, M. Sasaki, S. Sazonov, A. W. Strong, and J. Wilms. Detection of large-scale x-ray bubbles in the milky way halo. *Nature*, 588(7837):227–231, Dec. 2020. doi:10.1038/s41586-020-2979-0. URL <https://doi.org/10.1038/s41586-020-2979-0>.
- P. Predehl, R. Andritschke, V. Arefiev, V. Babyshkin, O. Batanov, W. Becker, H. Böhringer, A. Bogomolov, T. Boller, K. Borm, W. Bornemann, H. Bräuninger, M. Brüggén, H. Brunner, M. Brusa, E. Bulbul, M. Buntov, V. Burwitz, W. Burkert, N. Clerc, E. Churazov, D. Coutinho, T. Dauser, K. Dennerl, V. Doroshenko, J. Eder, V. Emberger, T. Eraerds, A. Finoguenov, M. Freyberg, P. Friedrich, S. Friedrich, M. Fürmetz, A. Georgakakis, M. Gilfanov, S. Granato, C. Grossberger, A. Gueguen, P. Gureev, F. Haberl, O. Hälker, G. Hartner, G. Hasinger, H. Huber, L. Ji, A. v. Kienlin, W. Kink, F. Korotkov, I. Kreykenbohm, G. Lamer, I. Lomakin, I. Lapshov, T. Liu, C. Maitra, N. Meidinger, B. Menz, A. Merloni, T. Mernik, B. Mican, J. Mohr, S. Müller, K. Nandra, V. Nazarov, F. Pacaud, M. Pavlinsky, E. Perinati, E. Pfeffermann, D. Pietschner, M. E. Ramos-Ceja, A. Rau, J. Reiffers, T. H. Reiprich, J. Robrade, M. Salvato, J. Sanders, A. Santangelo, M. Sasaki, H. Scheuerle, C. Schmid, J. Schmitt, A. Schwobe, A. Shirshakov, M. Steinmetz, I. Stewart, L. Strüder, R. Sunyaev, C. Tenzer, L. Tiedemann, J. Trümper, V. Voron, P. Weber, J. Wilms, and V. Yaroshenko. The eROSITA x-ray telescope on SRG. *Astronomy & Astrophysics*, 647:A1, Feb. 2021. doi:10.1051/0004-6361/202039313. URL <https://doi.org/10.1051/0004-6361/202039313>.
- K. C. Sarkar, B. B. Nath, and P. Sharma. Multiwavelength features of fermi bubbles as signatures of a galactic wind. *Monthly Notices of the Royal Astronomical Society*, 453(4):3828–3839, Sept. 2015. doi:10.1093/mnras/stv1806. URL <https://doi.org/10.1093/mnras/stv1806>.
- H.-Y. Schive, Y.-C. Tsai, and T. Chiueh. GAMER: A GRAPHIC PROCESSING UNIT ACCELERATED ADAPTIVE-MESH-REFINEMENT CODE FOR ASTROPHYSICS. *The Astrophysical Journal Supplement Series*, 186(2):457–484, feb 2010. doi:10.1088/0067-0049/186/2/457. URL <https://doi.org/10.1088/0067-0049/186/2/457>.
- H.-Y. Schive, J. A. ZuHone, N. J. Goldbaum, M. J. Turk, M. Gaspari, and C.-Y. Cheng. gamer-2: a GPU-accelerated adaptive mesh refinement code – accuracy, performance, and scalability. *Monthly Notices of the Royal Astronomical Society*, 481(4):4815–4840, 09 2018. ISSN 0035-8711. doi:10.1093/mnras/sty2586. URL <https://doi.org/10.1093/mnras/sty2586>.
- M. Selig, V. Vacca, N. Oppermann, and T. A. Enßlin. The de-noised, deconvolved, and decomposed Fermi-γ-ray sky. *Astronomy & Astrophysics*, 581:A126, Sept. 2015. doi:10.1051/0004-6361/201425172. URL <https://doi.org/10.1051/0004-6361/201425172>.
- S. L. Snowden, D. P. Cox, D. McCammon, and W. T. Sanders. A

- model for the distribution of material generating the soft x-ray background. *The Astrophysical Journal*, 354:211, May 1990. doi:10.1086/168680. URL <https://doi.org/10.1086/168680>.
- A. W. Strong, I. V. Moskalenko, and V. S. Ptuskin. Cosmic-ray propagation and interactions in the galaxy. *Annual Review of Nuclear and Particle Science*, 57(1):285–327, 2007. doi:10.1146/annurev.nucl.57.090506.123011. URL <https://doi.org/10.1146/annurev.nucl.57.090506.123011>.
- M. Su and D. P. Finkbeiner. EVIDENCE FOR GAMMA-RAY JETS IN THE MILKY WAY. *The Astrophysical Journal*, 753(1):61, June 2012. doi:10.1088/0004-637x/753/1/61. URL <https://doi.org/10.1088/0004-637x/753/1/61>.
- M. Su, T. R. Slatyer, and D. P. Finkbeiner. GIANT GAMMA-RAY BUBBLES FROM FERMI-LAT: ACTIVE GALACTIC NUCLEUS ACTIVITY OR BIPOLAR GALACTIC WIND? *The Astrophysical Journal*, 724(2):1044–1082, Nov. 2010. doi:10.1088/0004-637x/724/2/1044. URL <https://doi.org/10.1088/0004-637x/724/2/1044>.
- J. L. Synge. The Relativistic Gas. *North-Holland Pub. Co.; Interscience Publishers*, 1957.
- A. H. Taub. Relativistic Rankine-Hugoniot Equations. *Physical Review*, 74(3):328–334, Aug 1948. doi:10.1103/PhysRev.74.328.
- T. Tepper-García, J. Bland-Hawthorn, and R. S. Sutherland. THE MAGELLANIC STREAM: BREAK-UP AND ACCRETION ONTO THE HOT GALACTIC CORONA. *The Astrophysical Journal*, 813(2):94, Nov. 2015. doi:10.1088/0004-637x/813/2/94. URL <https://doi.org/10.1088/0004-637x/813/2/94>.
- P.-H. Tseng, H.-Y. Schive, and T. Chiueh. An adaptive mesh, GPU-accelerated, and error minimized special relativistic hydrodynamics code. *Monthly Notices of the Royal Astronomical Society*, 504(3):3298–3315, Apr. 2021. doi:10.1093/mnras/stab1006. URL <https://doi.org/10.1093/mnras/stab1006>.
- E. Valenti, M. Zoccali, A. Mucciarelli, O. A. Gonzalez, F. Surot, D. Minniti, M. Rejkuba, L. Pasquini, G. Fiorentino, G. Bono, R. M. Rich, and M. Soto. The central velocity dispersion of the milky way bulge. *A&AS*, 616:A83, Aug. 2018. doi:10.1051/0004-6361/201832905. URL <https://doi.org/10.1051/0004-6361/201832905>.
- A. Y. Wagner, G. V. Bicknell, and M. Umemura. DRIVING OUTFLOWS WITH RELATIVISTIC JETS AND THE DEPENDENCE OF ACTIVE GALACTIC NUCLEUS FEEDBACK EFFICIENCY ON INTERSTELLAR MEDIUM INHOMOGENEITY. *The Astrophysical Journal*, 757(2):136, Sept. 2012. doi:10.1088/0004-637x/757/2/136. URL <https://doi.org/10.1088/0004-637x/757/2/136>.
- H.-Y. K. Yang and M. Ruszkowski. The spatially uniform spectrum of the Fermi Bubbles: The leptonic active galactic nucleus jet scenario. *The Astrophysical Journal*, 850(1):2, Nov. 2017. doi:10.3847/1538-4357/aa9434. URL <https://doi.org/10.3847/1538-4357/aa9434>.
- H.-Y. K. Yang, M. Ruszkowski, P. M. Ricker, E. Zweibel, and D. Lee. THE FERMI BUBBLES: SUPERSONIC ACTIVE GALACTIC NUCLEUS JETS WITH ANISOTROPIC COSMIC-RAY DIFFUSION. *The Astrophysical Journal*, 761(2):185, Dec. 2012. doi:10.1088/0004-637x/761/2/185. URL <https://doi.org/10.1088/0004-637x/761/2/185>.
- R. Zhang and F. Guo. Simulating the fermi bubbles as forward shocks driven by AGN jets. *The Astrophysical Journal*, 894(2):117, May 2020. doi:10.3847/1538-4357/ab8bd0. URL <https://doi.org/10.3847/1538-4357/ab8bd0>.